Numerical heat transfer, Part A: applications, Volume 71, Issue 6, Pages 638 – 652
DOI: 10.1080/10407782.2017.1293985

Three-Dimensional Numerical Simulation of a Failed Coronary Stent Implant at Different Degree of Residual Stenosis. Part I: fluid dynamics and shear stress on the vascular wall.

Ivan Di Venuta[a], Andrea Boghi[b], Fabio Gori[a,*]

[a] Department of Industrial Engineering, University of Rome "Tor Vergata", Via del Politecnico 1, 00133 Rome, Italy.

[b] School of Water Energy, and Agrifood, Cranfield University, Cranfield, Bedfordshire MK43 0AL, United Kingdom,

[*] Corresponding Author, gori@uniroma2.it

Abstract

The influence of the degree of residual stenosis on the hemodynamics inside coronary arteries is investigated through three-dimensional (3D) numerical simulations. The present paper, which is the first of a series of two, focuses on the influence that the degree of residual stenosis (DOR) has on the fluid dynamics and the shear stresses acting on the stent and the artery wall. The pulsatile nature of the blood flow and its non-Newtonian features are taken into account. Four models of artery are investigated. The results show that the wall shear stress (WSS) increases monotonically, but not linearly, with the DOR.

Keywords: stent, stenosis, wall shear stress, Non-Newtonian.

Nomenclature

Latin

DOR	degree of restenosis.
j	imaginary unit.
J_o	zeroth-order Bessel function.
J_1	first-order Bessel function.
N	number of harmonics.
p	static pressure, Pa .
$\Re()$	real part of a complex number.
$R_{\max}$	maximum radius, m .
$R_{\min}$	minimum radius, m .
R_e	Reynolds number.
$[S]$	rate of the strain tensor, s^{-1}.
U_n	Fourier coefficients of the pulsatile mean velocity profile.
$\vec{v}$	fluid velocity, m/s .
WSS	wall shear stress, $dyne/cm^2$.

Greek

α_n Womersley numbers of order *n*.

$\dot{\gamma}$ shear rate, s^{-1}.

ρ density, kg/m^3.

$\xi = r/R$ dimensionless radial coordinate

1. Introduction

Cardiovascular diseases are the leading cause of death in the western world, accounting for the 50% of deaths occurring each year. Among these, the atherosclerosis is the most widespread. Several studies carried on during the last few decades have shown a correlation between cardiovascular diseases and specific flow conditions, such as stagnation of blood flow, and low and oscillatory wall shear stress (WSS) [1-3], suggesting that the stasis of blood flow and the fluid separation promote hyperplasia of the tunica intima, atherosclerosis and thrombi formation.

The stenosis of the coronary arteries is largely widespread and nowadays the most common clinical treatment is the stent implantation. The adoption of intravascular stents to restore the lumen of stenotic vessels has brought great improvements in term of quality of life in atherosclerotic patients. However, there are still some issues to be resolved. The main one is that the stent, recognized as a foreign body, lead to neointimal proliferation and subsequent synthesis of extracellular matrix components [4]. This uncontrolled proliferation can lead to restenosis of the vessel, and failure of the implant.

Drug-eluting stents (DES) are statistically superior to bare-metal stents (BMS) for the treatment of native coronary artery narrowing, having lower rates of major adverse cardiac events [5-6]. Nevertheless, the DES are unable to repair intima damaged by the stent implantation procedure, which can be limited by slightly oversized SE-BMS, [7]. Nonetheless, the residual stenosis present after the implant, even if not significant in terms of reduction of the flow rate, may represent a critical location for the hemodynamics. Moreover, there is good evidence that arterial injuries, caused by both balloons and stents, can lead to an inflammatory response, activating a proliferative repair process, which can provoke luminal narrowing and in-stent restenosis [8-10].

Alongside with the more traditional known risk factors, there is a strong evidence that the hemodynamics is also involved in the pathogenesis. Over the last few decades the use of computational fluid dynamics (CFD) in the biomedical field [11-12] and particularly in the blood flow simulation has received an increasing attention, because this technique is able to produce detailed 3D information of the hemodynamics. Both two-dimensional (2D) and three dimensional (3D) CFD simulations have been performed in arteries restored by stents. Two-dimensional CFD studies can be carried out to understand how these geometric features can be tuned to change the hemodynamics, employing simple stent geometries to investigate the influence of the mesh size on the blood flow, [13], the shape of the struts section, [14], and the design near the curvatures, [15].

LaDisa et al. [16-17], performed several 3D-CFD simulations on different geometries and stent design, analyzing how the 3D geometric parameters could affect the wall shear stress distribution. He et al. [18], studied a realistic strut geometry by considering three geometric parameters and showing that the stent

design is very important for the blood flow. Duraiswamy et al., [19], provided a physiologic rating on the effects of the stent geometry on the platelet deposition.

Most of the works treated blood as a Newtonian fluid except few studies that investigated the effect of the non-Newtonian behavior on the blood flow in a stenosed artery. Seo et al., [15], investigated the influence of the stent design close to curvatures, assuming a Carreau model. Benard et al., [20], investigated numerically the blood flow in arteries with rigid walls considering a Carreau-Yasuda relation. Amblard et al., [21], analyzed the phenomena of type I endo-leaks in a non-invasive-stented abdominal aorta with the Phan-Thien and Tanner models, derived from the rheology of polymer solutions. Non-Newtonian behavior of the fluid was investigated also in turbulent flow in [22-23], alongside with the characteristics of mass diffusion, [24-25]. Beier et al., [26], investigated the hemodynamic effect of shape characteristics, in particular bifurcation angle (BA), for non-stented and stented coronary arteries, also considering the non-Newtonian behavior on the blood flow. Martin et al., [27], studied the effect of the non-Newtonian character of the blood flow on the pulsatile flow conditions in both non-deformed geometrical models (NDF) and realistically-deformed (RDF) models of three stented coronary arteries. Rikhtegar et al., [28], studied the non-Newtonian blood flow in arteries with overlapping stents.

Gori et al. [29-31] carried out 3D-CFD simulations on commercial coronary stents, investigating the design features that can lead to pathological hemodynamics, and putting forward suggestions to avoid the failure of the implant. The fluid was considered Newtonian in [29, 31], while non-Newtonian features were investigated in [30]. Boghi and Gori [32] investigated the blood flow in two carotid arteries, SE-BMS, under physiologic conditions, and in an incompletely restored vessel lumen.

The aim of this work is to investigate the role of residual stenosis on the hemodynamics of stented coronary arteries. A simplified model of the artery, completely restored after stent implantation, is considered and, furthermore, three simplified models of not-completely restored coronary artery, with different degrees of residual stenosis (DOR), are investigated to study the potentially hazardous blood flow patterns that may arise from failure of the implant.

2. Geometry and Computational Grid

The stent geometry employed is relative to a patented Drug-Elutintg Stent [33] reconstructed with the commercial software SOLIDWORKS 2010. The vessel wall is modeled as a simple cylinder and the wall is considered rigid, which is a reasonable assumption, because the presence of the stent reduces the deformability of the wall. The cylinder representing the vessel has a diameter of 2.6 mm, according to [17], and a thickness of the stent of 0.1mm, according to the thickness of coronary stents, [8]. The length of the stent is 15 mm.

In order to perform a parametric study of the influence of residual stenosis, the other geometries employed for the simulation of the residual stenosis have a choking in the middle section, with a radius respectively of 1.09 mm, 0.82 mm and 0.45 mm, to which correspond a DOR equal to 30%, 60%, and 90% respectively. The DOR is defined by Eq. (1).

$$\mathrm{DOR}(\%) = 100\left(1 - \left(\frac{R_{\min}}{R_{\max}}\right)^2\right) \tag{1}$$

Figure 1 shows a comparison between the stent geometries with 0%, 30%, 60%, 90% of DOR.

The present work is aimed at characterizing the hemodynamics changes due to different DOR. Being the geometry periodic in the angular direction, it is possible to consider only a part of it by using the periodic boundary condition in Fluent. Two spatial pattern repetitions in the angular direction have been used to describe the phenomenon. A non-uniform grid, finer on the walls of the stent and the vessel, and coarser on the vessel center is employed to reduce the computational time. A grading is used to allow a smooth transition between the elements at the wall and those at the center. The periodicity of the vessel is set around the axis of the two periodic faces.

Three simulations with three grids of $8 \cdot 10^5$, $1.2 \cdot 10^6$ and $2.3 \cdot 10^6$ elements, shown in Fig. 2, are carried out to evaluate the most convenient size of the grid. The final grid used is that with $1.2 \cdot 10^6$ elements.

3. Governing equations

The blood is assumed as an incompressible Non-Newtonian fluid, with ρ = 1060 kg·m^{-3}, flowing in the coronary artery with a Reynolds number ranging from Re = 122 to 440, because of the pulsatile flow. The equations of mass and momentum conservations are respectively:

$$\mathrm{div}\left(\vec{v}\right) = 0 \tag{2}$$

$$\rho\frac{\partial\vec{v}}{\partial t} + \rho\vec{v}\cdot\nabla\vec{v} = -\nabla p + \mathrm{div}\left(2\mu\left(\dot{\gamma}\right)\left[S\right]\right) + \rho\vec{g} \tag{3}$$

The rate of the strain tensor is defined as:

$$\left[S\right] = \frac{\left(\left[\nabla\vec{v}\right] + \left[\nabla\vec{v}\right]^T\right)}{2} - \frac{1}{3}\mathrm{div}\left(\vec{v}\right)\left[I\right] \tag{4}$$

and the shear rate is:

$$\dot{\gamma} = \sqrt{2\left[S\right]:\left[S\right]} \tag{5}$$

In a Non-Newtonian fluid, the viscosity is a function of the shear rate and Eq.(3) is written in the Generalized Newtonian Fluid (GNF) form, derived from the constitutive equations of a *Reiner-Rivlin fluid* [34]. The blood viscosity is modeled with the Casson relation [35]. Further details are given in the second paper of this work, where the effect of the Casson viscosity is analyzed.

Equations (2-3) are solved under the boundary conditions of no slip on the artery and stent walls, rotational periodic for the two lateral surfaces of the cylinder, constant pressure on the outlet and prescribed mass flow rate at the inlet. Two different profiles are assumed for the mass flow rate: constant and pulsatile. The details of the pulsatile profile are discussed in the next section.

The simulations are performed by using the commercial software FLUENT, which solves the fluid-dynamics equations through the finite volume method (FVM). The SIMPLE algorithm is employed to solve

the pressure-velocity coupling and the simulations are carried out until the residuals reach the value of 10^{-6}. A second order implicit time-stepping method is used for the unsteady simulations, which run for two cardiac cycles, i.e. 1.6s, with a fixed time step of 0.8 ms. Only the second cycle results are recorded, while the first cycle is used to initialize the solution.

4. Transient simulations

In order to model the pulsatile blood flow in the unsteady state simulation, the Womersley-Evans theory [36] is used to obtain the velocity profile:

$$u(t,\xi) = u_s(\xi) + 2\Re\left(\sum_{n=1}^{N} U_n \Phi(\tau_n,\xi) e^{j\omega_n t}\right) \tag{6}$$

where

$$\Phi(\tau_n,\xi) = \frac{J_0(\tau_n) - J_0(\tau_n \xi)}{J_0(\tau_n) - 2J_1(\tau_n)/\tau_n} \tag{7}$$

and

$$\tau_n = j^{\frac{3}{2}} R\sqrt{\frac{\rho}{\mu_\infty}\omega_n} = j^{\frac{3}{2}}\alpha_n \tag{8}$$

By using the Fast Fourier Transform (FFT) algorithm, the mean value and the first 15 harmonics are extracted and used to reconstruct the velocity profile.

The physiological waveform suggested in [37] is assumed, as reported in Fig. 3. Finally, $u_s(\xi)$ is the steady state Casson velocity profile, which is essentially parabolic at the mean flow rate. The wave period is set equal to 0.8 s, corresponding to a heart rate of 75 bpm. As far as the velocity is concerned, its mean value is 0.16 m/s, which is the value used for steady state simulations. In particular, six significant time-instants were analyzed at t=0.2 s, t=0.3 s, t=0.4 s, t=0.5 s, t=0.6 s, t=0.8 s.

The wall shear stress (WSS) is the tangential drag force produced by the blood, which is moving across the endothelial surface, defined as

$$\overrightarrow{WSS} = 2\mu(\dot{\gamma})\left[\left[S\right]\cdot\hat{n} - \left(\hat{n}^T\cdot\left[S\right]\cdot\hat{n}\right)\hat{n}\right]\Big|_{wall} \tag{9}$$

The absolute value of the WSS is defined as $WSS = \left\|\overrightarrow{WSS}\right\|$. The unit of measurement used is dyne·cm^{-2}. The physiological range for the mean WSS value is of 5-70 dyne·cm^{-2} [12, 38-39].

5. Results

5.1 Grid Independence Study for steady state simulations

The Grid Independence study is performed using the results of the WSS, averaged over the vessel perimeter, which are shown in Fig. 4 for the geometries investigated, i.e. without residual stenosis and with 30%, 60% and 90% DOR. The solutions are validated with the use of the three grids reported in Fig. 2. More than 300 slices are generated by intersecting the vessel wall with parallel axial planes, and the resulting data

are interpolated by splines. Since the three grids offer similar results, the intermediate grid is used for the unsteady state simulations, as a compromise between accuracy and computational speed.

Figure 4a shows the results of the WSS in absence of DOR. A characteristic repeating peaks and valleys pattern is present, corresponding respectively to slices intersecting mostly the intra-strut area, i.e. where WSS is higher, and to those intersecting regions of low WSS, located on the struts. The WSS depends on the rate of shear, Eq.(9), which diminishes in proximity of the struts, due to the deceleration of the fluid impinging an obstacle, i.e. the struts, and the consequent formation of a recirculation region downstream the struts, whose amplitude depends on the Reynolds number. The presence of these recirculation regions increases the residence time of macrophages and macromolecules on the endothelium.

Figures 4b,c,d show the results of the average WSS in presence of the three different DOR. In general, the diameter reduction increases the local pressure drop and, consequently, accelerates the fluid. Since the WSS is, in first approximation, inversely proportional to the section diameter and directly proportional to the fluid velocity, it increases in the narrowing section. Downstream this region, the diameter increases and so the WSS diminishes. If the slope of the wall, downstream the narrowing, is sufficiently high, streamline detachment is present, and a consequent recirculation region which contributes to the lowering of WSS. In all the geometries with stenosis the maximum value of the WSS is registered upstream the maximum shrinkage of the section, i.e. in the middle of the domain, because both the axial and the transversal velocities change more rapidly upstream the maximum height of the stenosis.

Figure 4b shows the case with 30% of DOR. There is a local increase of WSS in proximity of the stenosis and a decrease below the physiological values downstream of it. Nevertheless, the values of the WSS are of the same order of magnitude of those shown in Fig. 4a, and the pattern of the repeating peaks and valleys, due to the struts, is still visible, despite the stenosis is the geometrical feature which leads to the highest WSS variation. Figure 4c reports the WSS in presence of a 60% DOR. In proximity of the stenosis the WSS increases about 3.5 times compared to the 30% DOR and 8.5 times compared to the case without stenosis. Downstream the stenosis there is a large recirculation region and the WSS drops considerably. A worst scenario is shown in Fig. 4d, where DOR is 90%. The WSS in proximity of the stenosis is 10 times higher, compared to 60% DOR, and the recirculation region is longer, meaning that the region of low WSS has a larger extent. For the geometries with 60% and 90% DOR, the stenosis causes a drop below the critical value of 5 dyne·cm^{-2} downstream of it and an amplification of the WSS in the central region where it exceeds 70 dyne·cm^{-2}, a critical value for which thrombogenic effects may occur [39].

5.2 Unsteady State Results.

The streamlines, obtained from the instantaneous velocity fields at four meaningful time steps and corresponding to four points of the mean velocity profile, are shown in Figs. 5-7 for the geometries with 30%, 60% and 90% DOR.

Figure 5 presents the streamlines for 30% DOR. The streamlines appear mostly parallel to the direction of the mean flow, even in proximity to the struts and during the systole, i.e. Fig. 5d, meaning that the recirculation, if exists, is very small. An exception to this behavior is at the diastole, Fig. 5a, when the fluid

proceeds backwards everywhere except downstream the stenosis at the center of the vessel, where a train of vortices can be seen. However, no vortex is seen on the vessel wall.

Figure 6 presents the streamlines for 60% DOR. The streamlines patterns are similar to the previous case, except downstream the stenosis, during the diastole, Fig. 6a, since the region interested by the train of vortices is wider. Figures 6b, c show streamlines mostly parallel to the direction of the mean flow and no near-wall vortex is visible. The near-wall vortices are present during the systole, Fig. 6d, downstream the stenosis, because the fluid at the narrowing is faster, and therefore more prone to generate near-wall vortices when the section expands. However, this effect disappears in 1.5 diameters, and the streamlines return parallel to the mean flow.

Figure 7 presents the streamlines for 90% DOR. The results in this case are different from the previous one. A large recirculation region is visible in the diastole, Fig. 7a, but with irregular contours. Figures 7b, c, d show that at the other three time steps, t=0.4 s, t=0.5 s, t=0.6 s, a wide recirculation region is present near the vessel wall and beyond the stenosis, and the flow on the vessel wall is directed upstream. This region of recirculation terminates several diameters downstream the end of the stent, and is not visible in the figures.

Figure 8 shows the WSS field for the geometry without residual stenosis at the instants of time indicated in Fig. 3. The WSS changes considerably during the cardiac cycle on the vascular wall, except in the zones adjacent to the stent, where the WSS is fairly constant and small, which make them permanently exposed to adverse conditions. As shown in Fig. 4a, the presence of the stent reduces the WSS, which drops below 5 dyne·cm^{-2}, a value at which the neo-intima hyperplasia is triggered, and the process of restenosis formation can take place. On the vascular wall, more distant from the struts, the WSS assumes physiological values throughout the cardiac cycle.

For the geometry with 30% DOR the results change considerably, as shown by Fig. 9. The region downstream the stenosis is subject to relatively small WSS, below 5 dyne·cm^{-2} for a longer period, while upstream it increases in comparison to the case without residual stenosis. Downstream the chocking, the WSS starts increasing when the flow rate returns to physiological conditions, far enough from the stenosis. This is the result of the increasing flow rate in correspondence to the section narrowing. In particular, this effect occurs when the flow rate is higher, while, for lower velocities, Fig. 9b, its pattern is similar to that in absence of residual stenosis.

Figure 10 reports the unsteady WSS in case of 60% DOR. The pattern of WSS is similar to that with 30% DOR, but the effect is more pronounced. The local WSS assumes very high values on the section of minimum area, especially during the systole, Fig. 10e, exceeding 70 dyne·cm^{-2}, which is the condition triggering thrombogenic effects [39]. Downstream this point, the WSS assumes very small values, below 5 dyne·cm^{-2}, for a longer period of time and larger extent compared to the previous case. Indeed, the stenosis is such that it promotes the formation of a recirculation region in the vascular endothelium, delimited by the periodic pattern of the struts. The areas where the fluid is more stagnant are critical and prone to a massive post-stent restenosis.

Finally, Fig. 11 shows the results for the geometry with 90% DOR. The WSS assumes hazardous values for most of the cardiac cycle, i.e. below 5 dyne·cm^{-2}, downstream the stenosis, and far above 70 dyne·cm^{-2} in correspondence with the chocking, which may lead to the occurrence of thrombogenic effects [39]. Beyond the stenosis, a wide recirculation region is formed, due to the high velocity of the blood in the necking, because of the large area reduction. The boundary layer detaches from the wall and reattaches several diameters downstream the contraction point. This effect may be due to the assumption of a straight long cylinder, while, in reality, the vessel has a certain curvature, and this phenomenon may be unlikely to occur.

6. Discussion

The present work analyses the Hemodynamics in a coronary stent with smooth symmetric residual stenosis. To the best of the authors' knowledge, this type of study has never been carried out before. Besides the fact that real residual stenosis may be asymmetrical, and with a steep profile, thus influencing the local WSS which can present larger values, the results of the present study can give a correct order of magnitude that cardiologists and the other specialized operators can expect from similar clinical scenarios. The present work reveals that the WSS distributions, in presence of residual stenosis, is highly asymmetrical, even if the residual stenosis is symmetrical, as pointed out in [32].

The presence of the stent reduces the local WSS, which can favour the infiltration of macrophages, especially in diastole, when WSS is often smaller than 5 dyne·cm^{-2}, as shown in [31-32]. The present investigation reports that in presence of high DOR, e.g. 60%-90%, the WSS becomes higher than in physiological conditions upstream the stenosis, even in the stent. For a DOR higher than 30% the WSS exceeds 70 dyne·cm^{-2}, which is the condition that triggers thrombogenic effects, [39].

For high DOR the region interested by critical WSS values is larger, and longer the time period when this condition occurs. In agreement with [32], the WSS drops considerably, below 5 dyne·cm^{-2}, downstream the stenosis, because the recirculation region increases with the DOR, and is stable because of the low Reynolds number. Certainly, in a real coronary this long region is not possible because of the vessel curvature. The case with 90% of DOR may be infrequent in the clinical practice, but can occur since stenosis can be asymptomatic up to 70% degree [40].

The analysis of the WSS is important in the evaluation of the stresses which the plaque is subject to. The rupture of the plaque depends on the break load, which, in turn, depends on the percent of calcification and lipids present. A possible conclusion is that the case with 60% and 90% of DOR show an increase in the WSS which can potentially breaks the plaque. The calculation of the stresses on the structure depend on the geometry and the rheology.

The present work has taken into account the Non-Newtonian behavior of the blood, whose influence on Hemodynamics, in non-completely restored coronary arteries, has never been studied. The Non-Newtonian rheology has an effect only when the flow rate is small, which is in the diastole. Therefore, this should not influence the rupture of the plaque. Nevertheless, this feature is relevant in determining the penetration of macro-molecules in the endothelium, which takes place for low and oscillatory WSS [38].

The discussion on this topic is very important because indicates the likelihood of the plaque growth. The wall permeability, as well as the influence of the non-Newtonian behaviour of the blood is discussed in the second paper of this work [41].

7. Conclusions

The influence of the Degree of residual stenosis (DOR) on the wall shear stress (WSS) in a stented coronary artery is investigated. The artery is assumed as an idealized cylindrical vessel and the stenosis has a smooth, axisymmetric shape. Three DOR are analyzed: 30%, 60%, and 90%, and the results are compared with those of a healthy stented artery. The Non-Newtonian behavior of the blood, modelled as a Casson fluid, is considered. The 3D numerical simulations show that for a DOR higher than 30% the WSS grows above 70 dyne·cm^{-2}, which may lead to thrombogenic effects. Moreover, even in absence of residual stenosis the WSS drops below 5 dyne·cm^{-2}, which is the value at which the neo-intima hyperplasia is triggered. For greater values of DOR the region interested by the critical condition is wider and longer the time of exposition. This condition is present at lower flow rates when the Non-Newtonian rheology is influent. In the second paper of this work, [41], the influence of the DOR on the wall permeability is investigated.

Acknowledgements

The authors thank Dr. Leon Williams of Cranfield University for the support given with SolidWorks.

References

1. C. Caro, J. Fitz-Gerald, R. Schroter, Arterial wall shear and distribution of early atheroma in man, *Nature*, (1969) 1159-1161.
2. C. Caro, J. Fitz-Gerald, R. Schroter, Atheroma: a new hypothesis, *British medical journal* 2 (5762) (1971) 651.
3. C. Caro, J. Fitz-Gerald, R. Schroter, Atheroma and arterial wall shear observation, correlation and proposal of a shear dependent mass transfer mechanism for atherogenesis, *Proceedings of the Royal Society of London B: Biological Sciences* 177 (1046) (1971) 109-133.
4. C. Walker, S. Stagg 3rd, Coronary stents: a review of recent developments, *The Journal of the Louisiana State Medical Society: official organ of the Louisiana State Medical Society* 142 (5) (1990) 25-32.
5. J.W. Moses, M.B. Leon, J.J. Popma, P.J. Fitzgerald, D.R. Holmes, C. O'Shaughnessy, R.P. Caputo, D.J. Kereiakes, D.O. Williams, P.S. Teirstein, et al., Sirolimus-eluting stents versus standard stents in patients with stenosis in a native coronary artery, *New England Journal of Medicine* 349 (14) (2003) 1315-1323.
6. G.W. Stone, S.G. Ellis, D.A. Cox, J. Hermiller, C. O'Shaughnessy, J.T. Mann, M. Turco, R. Caputo, P. Bergin, J. Greenberg, et al., One-year clinical results with the slow-release, polymer-based, paclitaxel-eluting taxus stent the taxus-iv trial, *Circulation* 109 (16) (2004) 1942-1947.
7. S.P. Lownie, D.M. Pelz, D.H. Lee, S.Men, I. Gulka, P. Kalapos, Efficacy of treatment of severe carotid bifurcation stenosis by using self-expanding stents without deliberate use of angioplasty balloons, *American journal of neuroradiology* 26 (5) (2005) 1241-1248.
8. Kastrati, J. Mehilli, J. Dirschinger, J. Pache, K. Ulm, H. Schühlen, M. Seyfarth, C. Schmitt, R. Blasini, F.-J. Neumann, et al., Restenosis after coronary placement of various stent types, *The American journal of cardiology* 87 (1) (2001) 34-39.
9. M. Schillinger, M. Exner, W. Mlekusch, M. Haumer, R. Ahmadi, H. Rumpold, O. Wagner, E. Minar, Inflammatory response to stent implantation: Differences in femoropopliteal, iliac, and carotid arteries 1, *Radiology* 224 (2) (2002) 529-535.
10. Farb, D.K.Weber, F.D. Kolodgie, A.P. Burke, R. Virmani, Morphological predictors of restenosis after coronary stenting in humans, *Circulation* 105 (25) (2002) 2974-2980.
11. S.W. Lee, D.S. Smith, F. Loth, P.F. Fisher, and H.S. Bassiouny, Numerical and experimental simulation of transitional flow in a blood vessel junction, *Numerical Heat Transfer, Part A: Applications* 51 (1) (2007) 1-22.
12. M. Fu, W. Weng, and Y. Hongyong, Numerical simulation of the effects of blood perfusion, water diffusion, and vaporization on the skin temperature and burn injuries, *Numerical Heat Transfer, Part A: Applications* 65 (12) (2014) 1187-1203.
13. J.L. Berry, A. Santamarina, J.E. Moore, S. Roychowdhury, W.D. Routh, Experimental and computational fow evaluation of coronary stents, *Annals of biomedical engineering* 28 (4) (2000) 386-398.

14. L. Lanoye, M. De Beule, C. Dewijngaert, P. Segers, P. Van Impe, and P. Verdonck, The Influence of the Strut Section Shape on the Flow Field in a Newly Stented Right Coronary Artery, *The 56th National Congress of Theoretical and Applied Mechanics, NCTAM, 2006.*
15. T. Seo, L.G. Schachter, A.I. Barakat, Computational study of fluid mechanical disturbance induced by endovascular stents, *Annals of biomedical engineering* 33 (4) (2005) 444-456.
16. J.F. LaDisa, L.E. Olson, I. Guler, D.A. Hettrick, S.H. Audi, J.R. Kersten, D.C. Warltier, P.S. Pagel, Stent design properties and deployment ratio influence indexes of wall shear stress: a three-dimensional computational fluid dynamics investigation within a normal artery, *Journal of Applied Physiology* 97 (1) (2004) 424-430.
17. J.F. LaDisa, D.A. Hettrick, L.E. Olson, I. Guler, E.R. Gross, T.T. Kress, J.R. Kersten, D.C. Warltier, P.S. Pagel, Stent implantation alters coronary artery hemodynamics and wall shear stress during maximal vasodilation, *Journal of Applied Physiology* 93 (6) (2002) 1939-1946.
18. Y. He, N. Duraiswamy, A.O. Frank, J.E. Moore, Blood flow in stented arteries: a parametric comparison of strut design patterns in three dimensions, *Journal of biomechanical engineering* 127 (4) (2005) 637-647.
19. N. Duraiswamy, J.M. Cesar, R.T. Schoephoerster, J.E. Moore Jr, Effects of stent geometry on local flow dynamics and resulting platelet deposition in an in vitro model, *Biorheology* 45 (5) (2008) 547-561.
20. N. Benard, R. Perrault, D. Coisne, Computational approach to estimating the effects of blood properties on changes in intra-stent flow, *Annals of biomedical engineering* 34 (8) (2006) 1259-1271.
21. Amblard, H. Walter-Le Berre, B. Bou-Saïd, M. Brunet, Analysis of type i endoleaks in a stented abdominal aortic aneurysm, *Medical engineering & physics* 31 (1) (2009) 27-33.
22. F. Gori, A. Boghi, Two new differential equations of turbulent dissipation rate and apparent viscosity for non-newtonian fluids, *International Communications in Heat and Mass Transfer* 38 (6) (2011) 696-703.
23. F. Gori, A. Boghi, A three dimensional exact equation for the turbulent dissipation rate of generalised newtonian fluids, *International Communications in Heat and Mass Transfer* 39 (4) (2012) 477-485.
24. F. Gori, A. Boghi, On a new passive scalar equation with variable mass diffusivity, in: *ASME 2008 International Mechanical Engineering Congress and Exposition, American Society of Mechanical Engineers*, (2008) 495-500.
25. F. Gori, A. Boghi, On a new passive scalar equation with variable mass diffusivity: Flow between parallel plates, *Journal of Fluids Engineering* 132 (11) (2010) 111202.
26. S. Beier, J. Ormiston, M. Webster, J. Cater, S. Norris, P. Medrano-Gracia, A. Young, B. Cowan, Impact of bifurcation angle and other anatomical characteristics on blood flow-a computational study of non-stented and stented coronary arteries, *Journal of biomechanics* 49 (9) (2016) 1570-1582.
27. D.M. Martin, E.A. Murphy, F.J. Boyle, Computational fluid dynamics analysis of balloon-expandable coronary stents: influence of stent and vessel deformation, *Medical engineering & physics* 36 (8) (2014) 1047-1056.

28. F. Rikhtegar, C. Wyss, K.S. Stok, D. Poulikakos, R. Müller, V. Kurtcuoglu, Hemodynamics in coronary arteries with overlapping stents, *Journal of biomechanics* 47 (2) (2014) 505-511.
29. F. Gori, A. Boghi, M. Amitrano, Three-dimensional numerical simulation of the fluid dynamics in a coronary stent, *ASME 2009 International Mechanical Engineering Congress and Exposition, American Society of Mechanical Engineers*, (2009) 407-411.
30. F. Gori, A. Boghi, Three-dimensional numerical simulation of non-newtonian blood in two coronary stents, *14th International Heat Transfer Conference, American Society of Mechanical Engineers*, (2010) 109-114.
31. F. Gori, A. Boghi, Three-dimensional numerical simulation of blood flow in two coronary stents, *Numerical Heat Transfer, Part A: Applications* 59 (4) (2011) 231-246.
32. Boghi, F. Gori, Numerical simulation of blood flow through different stents in stenosed and non-stenosed vessels, *Numerical Heat Transfer, Part A: Applications* 68 (3) (2015) 225-242.
33. S. Robaina, C. Hitzman, K. Robertson, L. Davis, J.T. Lenz, Drug-eluting stent, US Patent 7,951,193 (May 31 2011).
34. G. Astarita, G. Marrucci, *Principles of non-Newtonian fluid mechanics*, Vol. 28, McGraw-Hill New York, 1974.
35. Fournier, Ronald L. *Basic transport phenomena in biomedical engineering*, pp. 122-139, CRC Press, 2011.
36. J.R. Womersley, Method for the calculation of velocity, rate of flow and viscous drag in arteries when the pressure gradient is known, *The Journal of physiology* 127 (3) (1955) 553.
37. R.M. Berne, M.N. Levy, *Cardiovascular physiology*, Mosby, 1967.
38. D.N. Ku, D.P. Giddens, C.K. Zarins, S. Glagov, Pulsatile flow and atherosclerosis in the human carotid bifurcation. positive correlation between plaque location and low oscillating shear stress, *Arteriosclerosis, thrombosis, and vascular biology* 5 (3) (1985) 293-302.
39. A.M. Malek, S.L. Alper, S. Izumo, Hemodynamic shear stress and its role in atherosclerosis, *Jama* 282 (21) (1999) 2035-2042.
40. T.D. Singh, C.L. Kramer, J. Mandrekar, G. Lanzino, A. Rabinstein, Asymptomatic carotid stenosis: Risk of progression and development of symptoms, *Cerebrovascular Diseases* 40 (5-6) (2015) 236-243.
41. Boghi, I. Di Venuta, F. Gori, Three-dimensional numerical simulation of a failed coronary stent implant at different degree of residual stenosis. Part II: apparent viscosity and wall permeability, *Numerical Heat Transfer*, submitted for publication.

Caption to Figures

Figure 1 - Stent geometries with: (a) 0 % DOR, (b) 30 % DOR, (c) 60 % DOR, (d) 90 % DOR.

Figure 2 – Computational Grid with: (a) $8 \cdot 10^5$ *elements, (b)* $1.2 \cdot 10^6$ *elements, (c)* $2.3 \cdot 10^6$ *elements.*

Figure 3 - Mean Velocity profile for a human left coronary vessel.

Figure 4 - Grid Independence with average WSS versus axial length. (a) 0% DOR, (b) 30% DOR, (c) 60% DOR and (d) 90% DOR.

Figure 5- Streamlines for the geometry with 30% DOR during the cardiac cycle: a) t=0.3s (diastole), b) t=0.4s, c) t=0.5s, d) t=0.6s (systole)

Figure 6 - Streamlines for the geometry with 60% DOR during the cardiac cycle: a) t=0.3s (diastole), b) t=0.4s), c) t=0.5s, d) t=0.6s (systole)

Figure 7 - Streamlines for the geometry with 90% DOR during the cardiac cycle: a) t=0.3s (diastole), b) t=0.4s, c) t=0.5s, d) t=0.6s (systole)

Figure 8 - Local WSS during the cardiac cycle for the geometry without residual stenosis. a) t=0.2s, b) t=0.3s (diastole), c) t=0.4s, d) t=0.5s, e) t=0.6s (systole), f) t=0.8s.

Figure 9 - Local WSS during the cardiac cycle for the geometry with 30% DOR: a) t=0.2s, b) t=0.3s (diastole), c) t=0.4s, d) t=0.5s, e) t=0.6s (systole), f) t=0.8s.

Figure 10 - Local WSS during the cardiac cycle for the geometry with 60% DOR: a) t=0.2s, b) t=0.3s (diastole), c) t=0.4s, d) t=0.5s, e) t=0.6s (systole), f) t=0.8s.

Figure 11 - Local WSS during the cardiac cycle for the geometry with 90% DOR: a) t=0.2s, b) t=0.3s (diastole), c) t=0.4s, d) t=0.5s, e) t=0.6s (systole), f) t=0.8s.

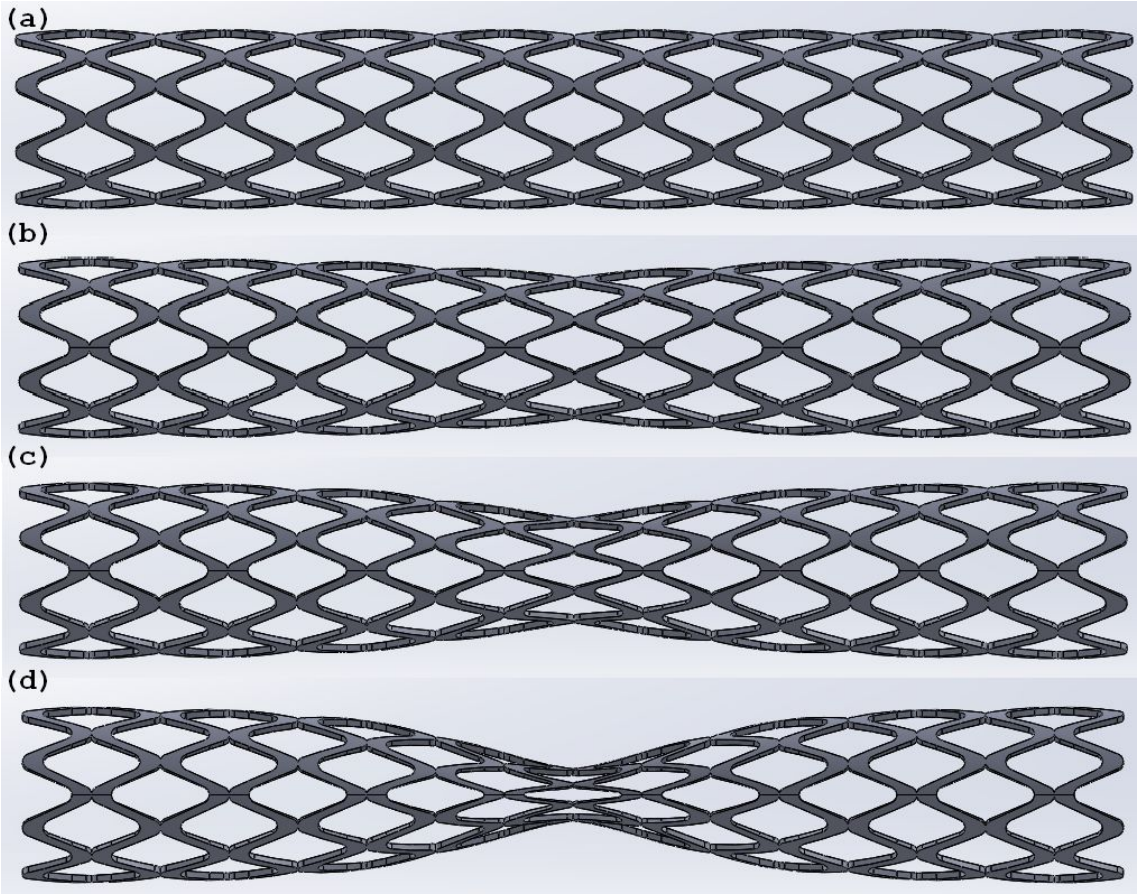

Figure 1 - Stent geometries with: (a) 0 % DOR, (b) 30 % DOR, (c) 60 % DOR, (d) 90 % DOR.

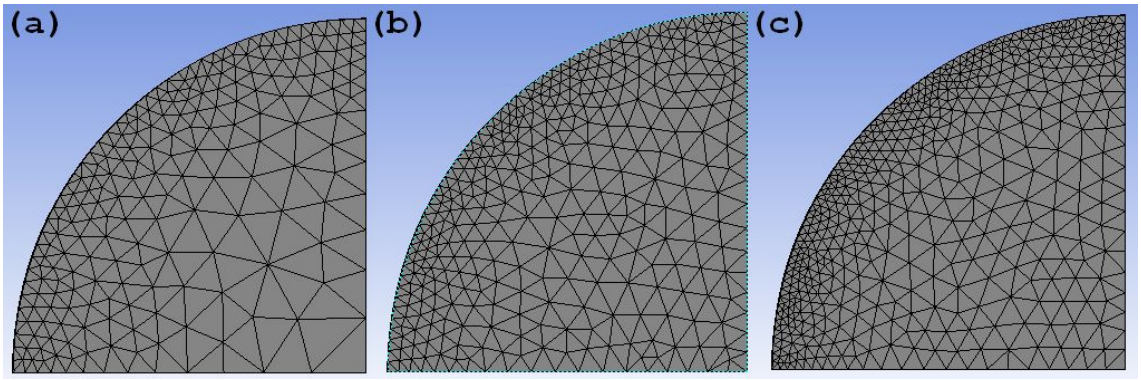

Figure 2 – Computational Grid with: (a) $8 \cdot 10^5$ *elements, (b)* $1.2 \cdot 10^6$ *elements, (c)* $2.3 \cdot 10^6$ *elements.*

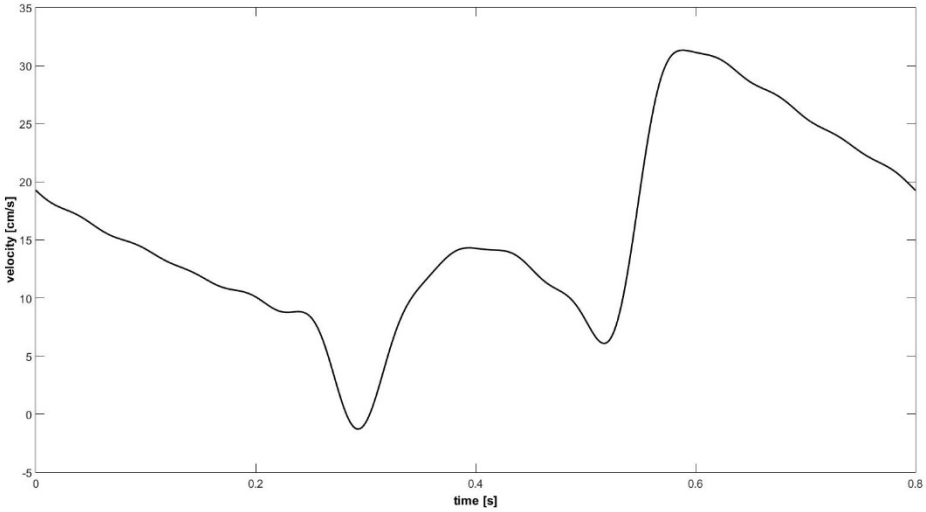

Figure 3 - Mean Velocity profile for a human left coronary vessel.

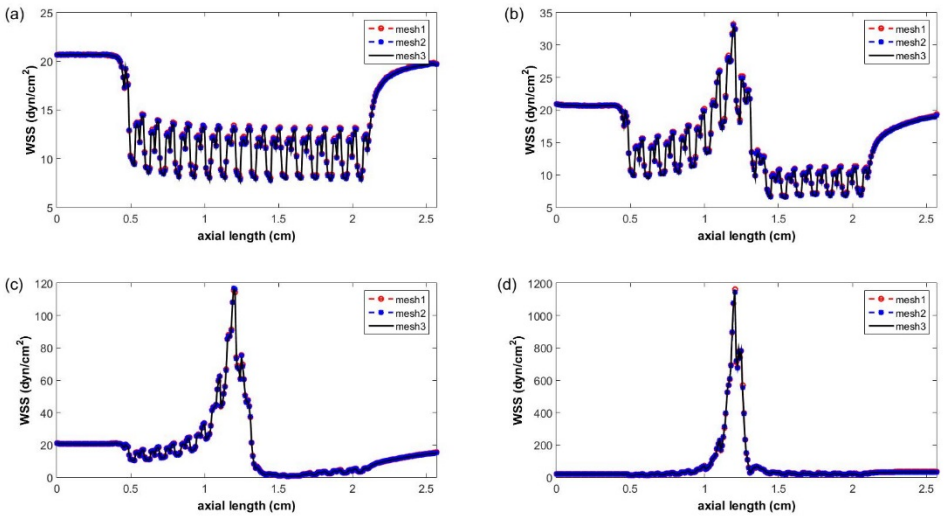

Figure 4 - Grid Independence with average WSS versus axial length. (a) 0% DOR, (b) 30% DOR, (c) 60% DOR and (d) 90% DOR.

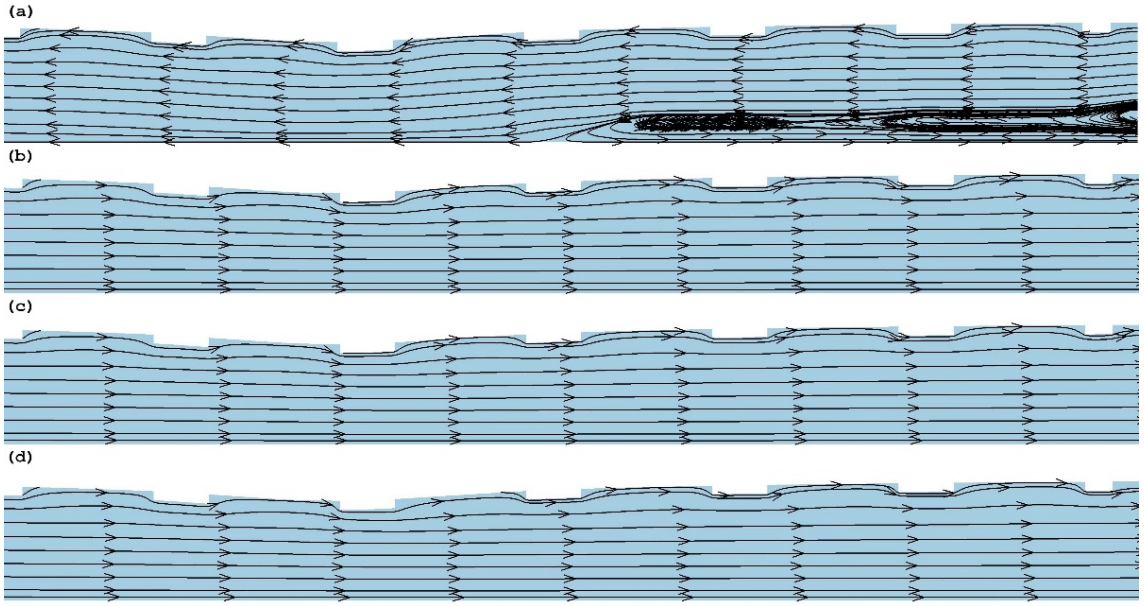

Figure 5- Streamlines for the geometry with 30% DOR during the cardiac cycle: a) t=0.3s (diastole), b) t=0.4s, c) t=0.5s, d) t=0.6s (systole)

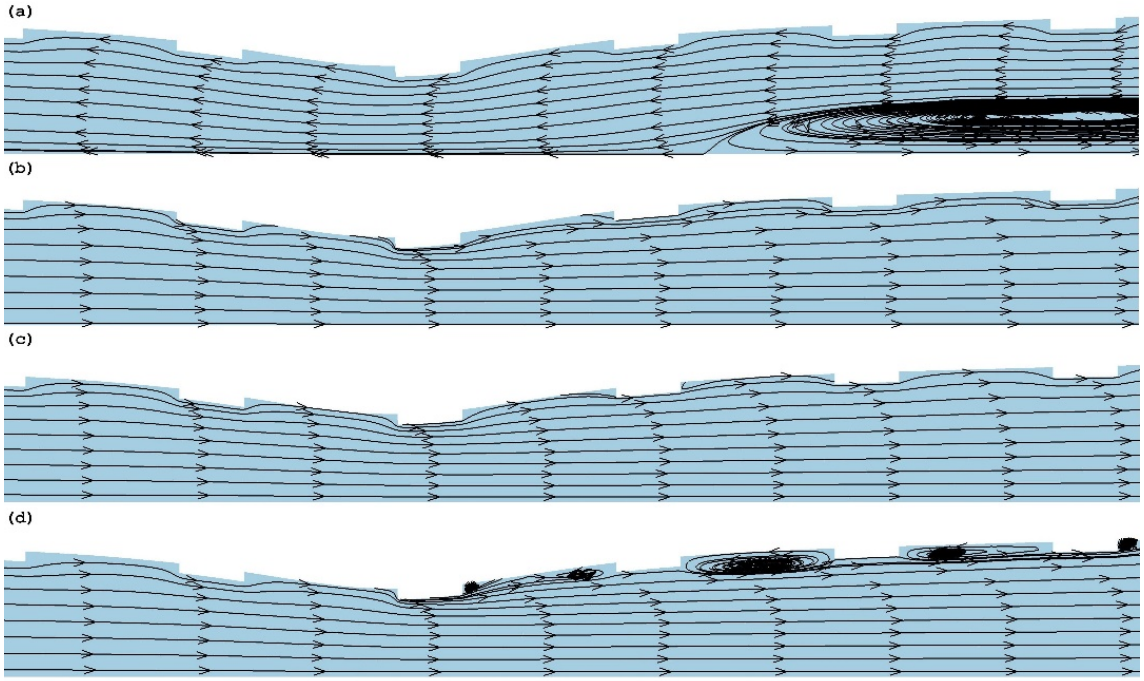

Figure 6 - Streamlines for the geometry with 60% DOR during the cardiac cycle: a) t=0.3s (diastole), b) t=0.4s), c) t=0.5s, d) t=0.6s (systole)

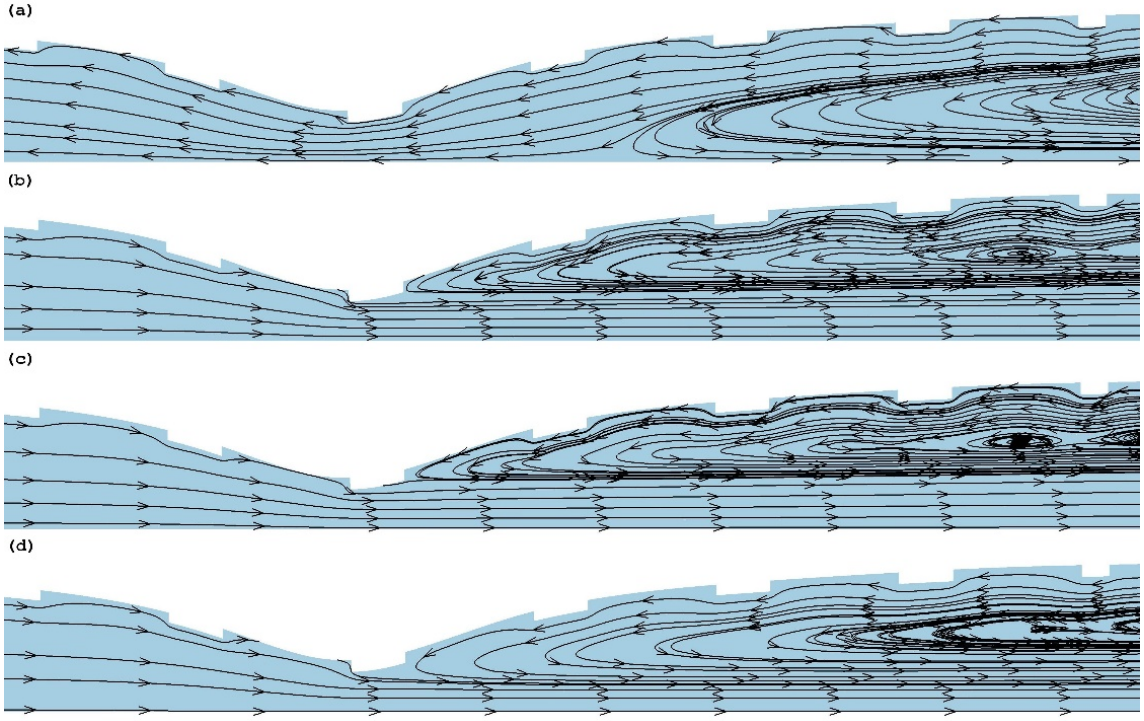

Figure 7 - Streamlines for the geometry with 90% DOR during the cardiac cycle: a) t=0.3s (diastole), b) t=0.4s, c) t=0.5s, d) t=0.6s (systole)

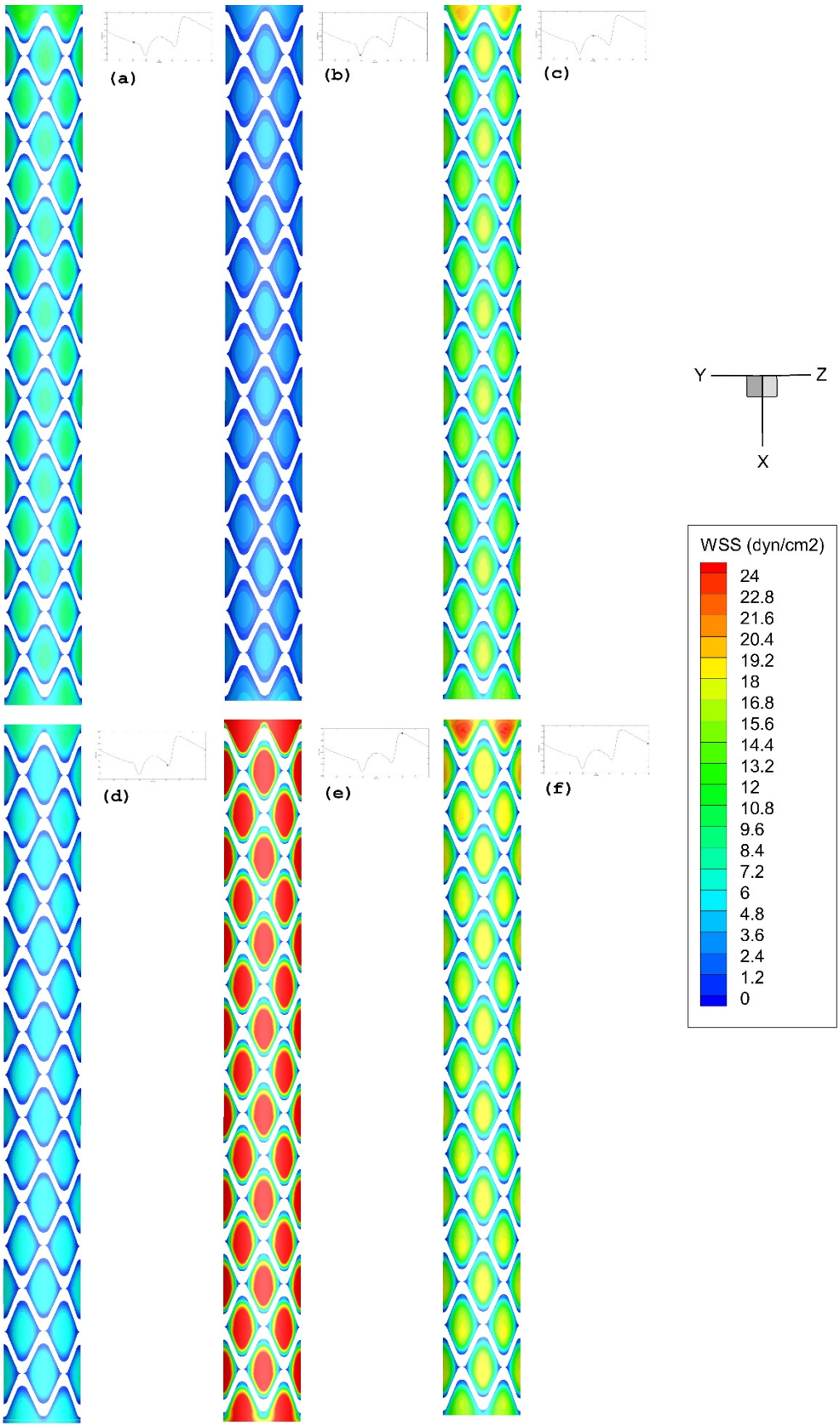

Figure 8 - Local WSS during the cardiac cycle for the geometry without residual stenosis. a) t=0.2s, b) t=0.3s (diastole), c) t=0.4s, d) t=0.5s, e) t=0.6s (systole), f) t=0.8s.

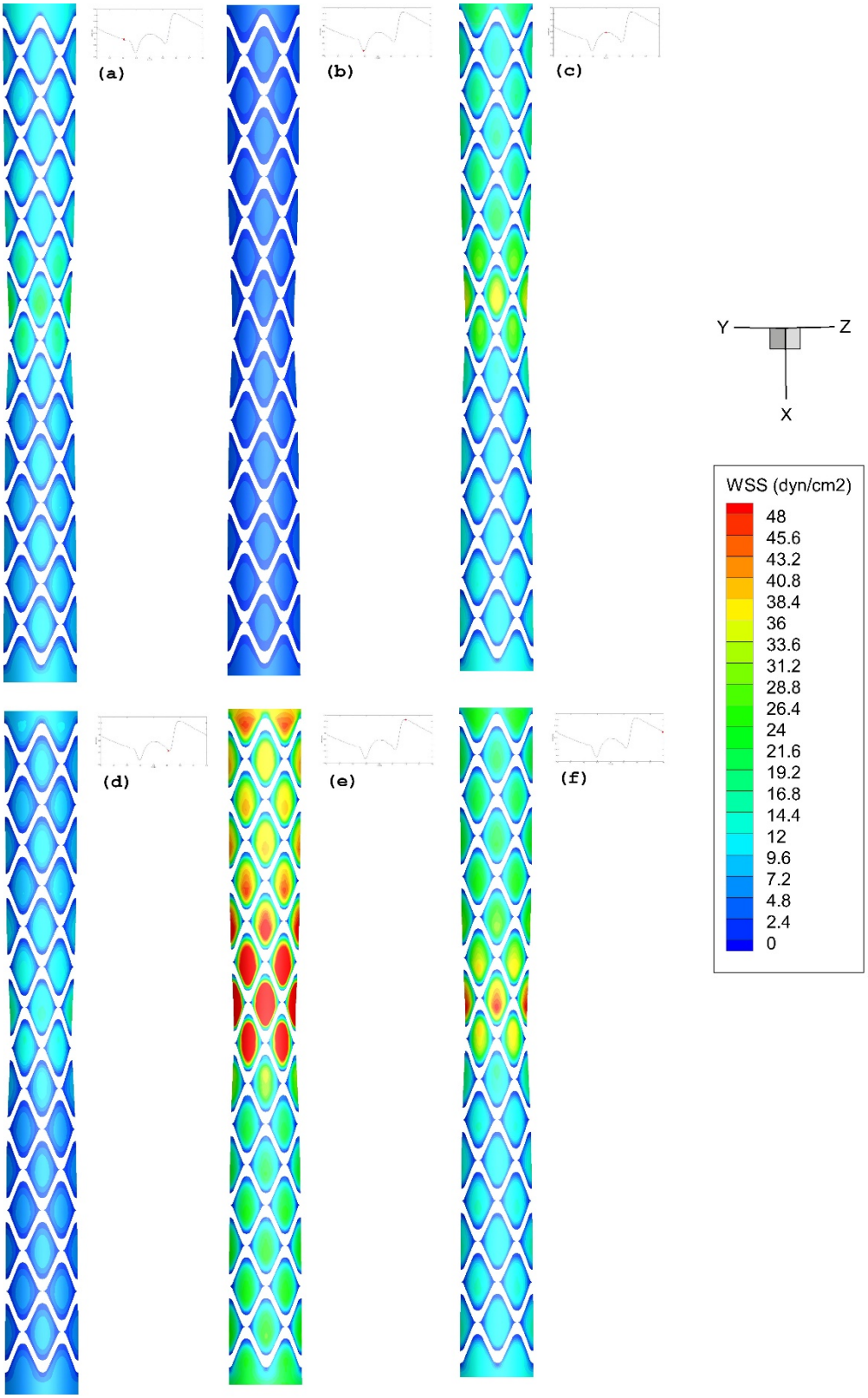

Figure 9 - Local WSS field during the cardiac cycle for the geometry with 30% DOR. a) t=0.2s, b) t=0.3s (diastole), c) t=0.4s, d) t=0.5s, e) t=0.6s (systole), f) t=0.8s.

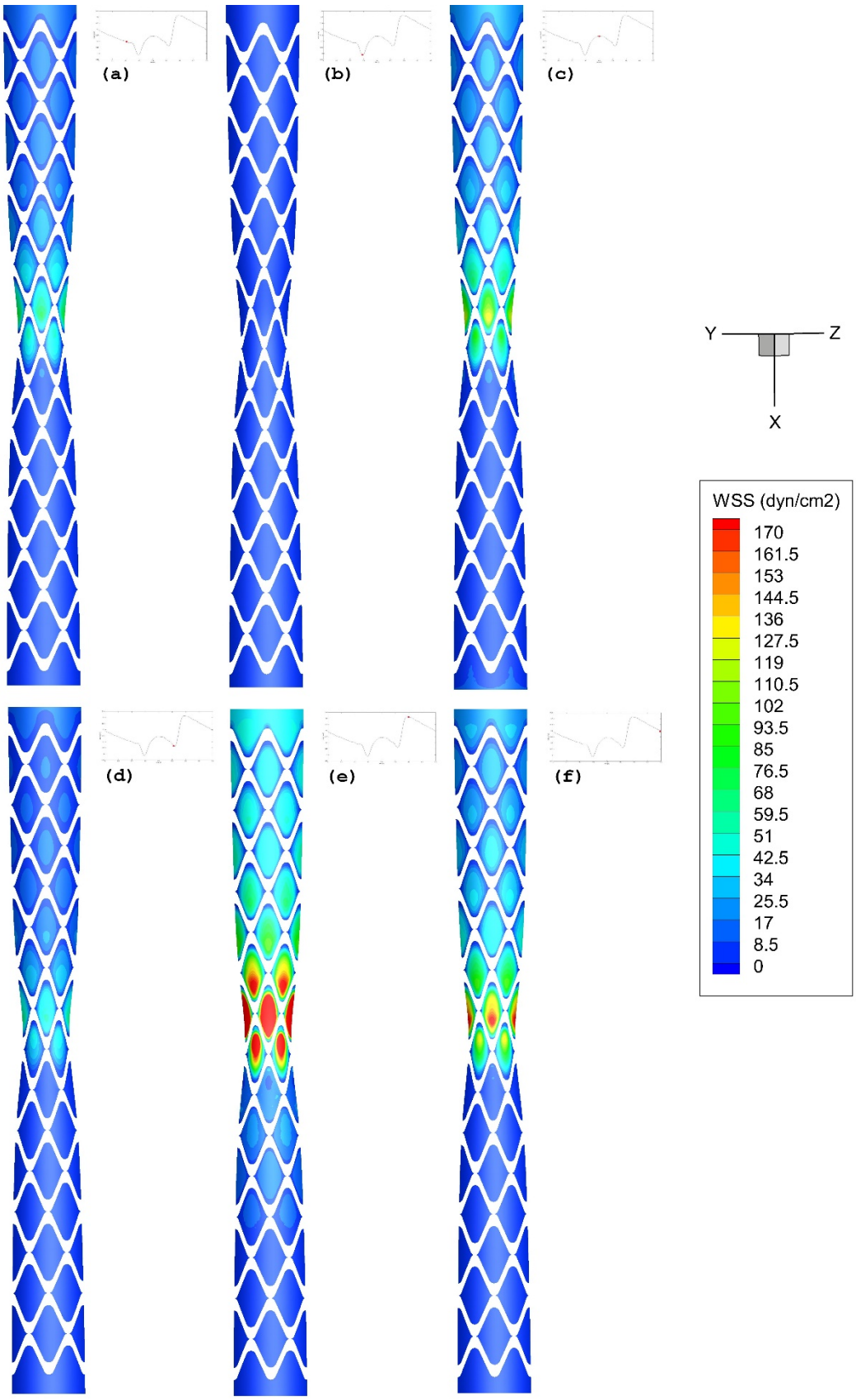

Figure 10 - Local WSS field during the cardiac cycle for the geometry with 60% DOR. a) t=0.2s, b) t=0.3s (diastole), c) t=0.4s, d) t=0.5s, e) t=0.6s (systole), f) t=0.8s.

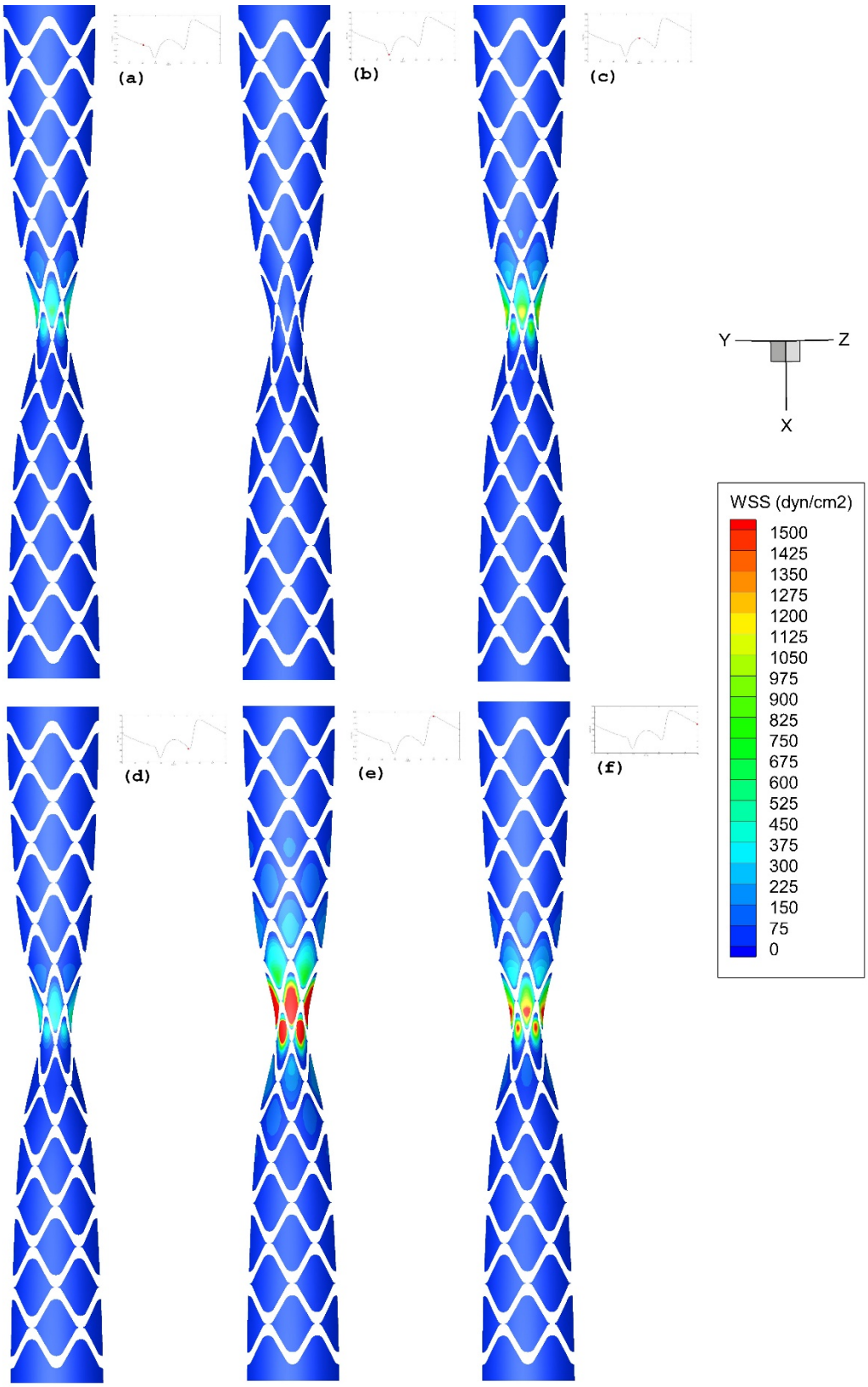

Figure 11 - Local WSS field during the cardiac cycle for the geometry with 90% DOR. a) t=0.2s, b) t=0.3s (diastole), c) t=0.4s, d) t=0.5s, e) t=0.6s (systole), f) t=0.8s.